

X-Ray and Near-Infrared Observations of GX 339–4 in the Low/Hard State with Suzaku and IRSF

Megumi SHIDATSU¹, Yoshihiro UEDA¹, Fumie TAZAKI¹, Tatsuhito YOSHIKAWA¹,
Takahiro NAGAYAMA², Tetsuya NAGATA¹, Nagisa OI³, Kazutaka YAMAOKA⁴,
Hiromitsu TAKAHASHI⁵, Aya KUBOTA⁶, Jean COTTAM⁷, Ronald REMILLARD⁸, and Hitoshi NEGORO⁹

¹*Department of Astronomy, Kyoto University, Kyoto 606-8502*

shidatsu@kustastro.kyoto-u.ac.jp

ueda@kustastro.kyoto-u.ac.jp

²*Department of Astrophysics, Nagoya University, Aichi 464-8602*

³*Department of Astronomy, Graduate University for Advanced Studies, Tokyo 181-8588*

⁴*Department of Physics, Aoyama Gakuin University, Kanagawa 229-8558*

⁵*Department of Physical Science, Hiroshima University, Hiroshima 739-8526*

⁶*Department of Electronic Information Systems, Shibaura Institute of Technology, Saitama 337-8570*

⁷*Exploration of the Universe Division, NASA Goddard Space Flight Center, Greenbelt, MD 20771, USA*

⁸*Department of Physics, Massachusetts Institute of Technology, Cambridge, MA 02138, USA*

⁹*Department of Physics, Nihon University, Tokyo 101-8308*

(Received 2011 March 29; accepted 2011 May 17)

Abstract

X-ray and near-infrared (J - H - K_s) observations of the Galactic black hole binary GX 339–4 in the low/hard state were performed with Suzaku and IRSF in 2009 March. The spectrum in the 0.5–300 keV band is dominated by thermal Comptonization of multicolor disk photons, with a small contribution from a direct disk component, indicating that the inner disk is almost fully covered by hot corona with an electron temperature of ≈ 175 keV. The Comptonizing corona has at least two optical depths, $\tau \approx 1, 0.4$. Analysis of the iron-K line profile yields an inner disk radius of $(13.3^{+6.4}_{-6.0})R_g$ (R_g represents the gravitational radius GM/c^2), with the best-fit inclination angle of $\approx 50^\circ$. This radius is consistent with that estimated from the continuum fit by assuming the conservation of photon numbers in Comptonization. Our results suggest that the standard disk of GX 339–4 is likely truncated before reaching the innermost stable circular orbit (for a non rotating black hole) in the low/hard state at $\sim 1\%$ of the Eddington luminosity. The one-day averaged near-infrared light curves are found to be correlated with hard X-ray flux with $F_{K_s} \propto F_X^{0.45}$. The flatter near infrared νF_ν spectrum than the radio one suggests that the optically thin synchrotron radiation from the compact jets dominates the near-infrared flux. Based on a simple analysis, we estimate the magnetic field and size of the jet base to be 5×10^4 G and 6×10^8 cm, respectively. The synchrotron self Compton component is estimated to be approximately 0.4% of the total X-ray flux.

Key words: accretion, accretion disks — black hole physics — infrared: stars — stars: individual (GX 339–4) — X-rays: binaries

1. Introduction

Black hole binaries (BHBs), a class of the brightest Galactic X-ray sources, are ideal objects to study the accretion disk physics around a black hole. They exhibit distinct “states” with different luminosity and spectral shape, which are mainly determined by the mass accretion rate (see e.g., Done et al. 2007 for a recent review). When the accretion rate is high (but below several 10% of the Eddington limit), the spectra of BHBs are dominated by a soft X-ray component below 10 keV. This state is called the “high/soft” state, and its dominant soft component is described by a Multi-Color Disk (MCD) model, formed by a superposition of blackbody radiation at different temperatures emitted from various radii of the disk (Mitsuda et al. 1984). In this state, many observations

suggest that the disk is extending down to the innermost stable circular orbit (ISCO).

In contrast, at lower accretion rates, the hard X-ray (> 10 keV) contribution to the entire flux becomes more substantial. This state, called the “low/hard” state, shows X-ray spectra approximated by a power law of photon index 1.5–1.9 with a high energy cut-off at ~ 100 keV. This emission is interpreted to be produced by unsaturated Compton up-scattering by hot electrons of seed photons emitted by the disk. The physical properties and geometry of the corona in relation to the disk, however, remain to be studied. While there is a consensus that an optically thick disk is truncated before reaching the ISCO at low mass accretion rates (e.g., Esin et al. 1997), discussion at what Eddington fraction the disk becomes truncated is still controversial (see below).

Radio to optical observations of BHBs have provided evidence for the presence of stable jets in the low/hard state, while the jet is quenched in the high/soft state (Fender et al. 1999a). By using radio interferometers, the central compact core and jet-like knots are resolved in several BHBs in the low/hard state (Fender 2001, and references therein). In the radio region, the spectral energy distribution (SED) of BHBs exhibits an almost flat profile, which is considered to be optically thick synchrotron radiation from the jets, like those observed from active galactic nuclei (Blandford & Königl 1979). This flat spectrum is thought to extend to the sub-mm or infrared wavelengths, above which the synchrotron emission becomes optically thin and eventually declines as a power law with an index > 1 (SED units). Thus, observations at the wavelengths where the synchrotron luminosity from the jets peaks give key information to understand the energetics of the jet.

GX 339–4 is a transient Galactic BHB, discovered in the early 1970s (Markert et al. 1973). Although this object was observed for many years at various wavelengths, its binary-system parameters are still uncertain (see Section 2). The accretion disk geometry in the low/hard state has been studied from X-ray spectra at different luminosities. Tomsick et al. (2009) show that, at ~ 0.001 of the Eddington luminosity (L_{Edd}), the standard disk is truncated at $> 35R_g$ ($R_g \equiv GM/c^2$ is the gravitational radius, where G , M , and c are the gravitational constant, black hole mass, and light velocity, respectively.) Miller et al. 2006 argue that the disk extends to $\approx 4R_g$ in the bright low/hard state at ~ 0.06 of the Eddington luminosity, based on the detection of a broad iron-K emission line. Similar results are reported by Tomsick et al. (2008) at $0.023L_{\text{Edd}}$ and $0.008L_{\text{Edd}}$. Done & Diaz Trigo (2010), however, re-analyze the same data used by Miller et al. (2006), and find that the spectra are strongly affected by pile-up (multiple photon events in CCD). Extracting the simultaneous data that are free from pile-up, they obtain a narrower iron-K line profile that rather favors a truncated disk with an innermost radius of $> 6R_g$. Thus, the disk evolution of GX 339–4 in the low/hard state as a function of luminosity is not firmly established yet. GX 339–4 is also a persistent radio source in the low/hard state, whose spectrum is flat or slightly increases according to the frequency with the spectral index $\approx +0.1$ – 0.2 (Corbel et al. 2000). In spite of the importance of the near-infrared data, simultaneous multi-band observations in the J - H - K bands and X-rays have been very limited so far.

To establish the inner disk structure of BHBs in the low/hard state, we observed GX 339–4 using the X-ray satellite Suzaku in 2009 March, when it became active and stayed in the low/hard state. Quasi-simultaneous near-infrared observations were performed with the Infrared Survey Facility (IRSF) 1.4 m telescope to reveal the jet activity. In this paper, we first summarize the constraints on the system parameters of GX 339–4 based on previous observations in Section 2. The Suzaku observations and data reduction are described in Section 3, and analysis of the X-ray data is given in Section 4. In Section 5, we

present details of the IRSF observations and data analysis. We discuss our X-ray and near-IR results by comparing with previous observations of GX 339–4 and other BHBs in Section 6. The conclusions are summarized in Section 7.

2. Summary of Constraints on Inclination and Distance of GX 339–4

The system parameters of GX 339–4 including the distance, inclination angle, black hole mass (hereafter M_{BH}), and the mass of companion star (M_{C}) are still unknown. Figure 1 summarizes the constraints derived from previous observations in the inclination (or black hole mass) versus distance plane. The limit that i is less than $\sim 60^\circ$ is imposed by the fact that GX 339–4 exhibits no eclipse (Cowley et al. 2002). The upper and lower limits of the distance D are estimated in several different ways. Zdziarski et al. (1998) found that $D > 3$ kpc by investigating the interstellar reddening, while Hynes et al. (2004) estimated $6 \text{ kpc} < D < 15 \text{ kpc}$ using the structure of Na D line obtained through high-resolution spectroscopy. Zdziarski et al. (2004) put the limit $7 \text{ kpc} < D < 9 \text{ kpc}$, using the apparent radius of the secondary low-mass star based on optical and infrared observations. In Figure 1, we plot the Hynes et al. (2004) and Zdziarski et al. (1998) results for the upper and lower limits of the distance, respectively.

The dependence of M_{BH} on the inclination angle is obtained from the mass function, which is expressed as

$$f(M_{\text{BH}}) = \frac{M_{\text{BH}}}{(1 + \frac{M_{\text{C}}}{M_{\text{BH}}})^2} \sin^3 i = \frac{PK_{\text{C}}^3}{2\pi G}, \quad (1)$$

where P , G , and K_{C} are the orbital period, the gravitational constant, and the radial velocity semi-amplitude of the companion star, respectively. Hynes et al. (2003) estimated $f(M_{\text{BH}})$ of GX 339–4 to be $5.8 M_{\odot}$ ($2.0 M_{\odot}$ at a 95% confidence lower limit) by observing the Doppler shifts of the N III and He II emission lines from the irradiated companion star. Ignoring the $M_{\text{C}}/M_{\text{BH}}$ term in Equation 1, whose value is less than 0.08 according to Zdziarski et al. (2004), we calculate the black hole mass corresponding to each inclination angle, which is indicated in the upper axis.

For a given $f(M_{\text{BH}})$ value, we can also constrain the relation between the distance and inclination angle, assuming that the fraction of the Eddington luminosity in the very high state should be in the range of $0.1 \lesssim L/L_{\text{Edd}} \lesssim 1$. Here we refer to the 0.2–100 keV luminosity in the very high state obtained with Suzaku in 2007 (Yamada et al. 2009), $3.8 \times 10^{38} (D/8 \text{ kpc})^2 \text{ erg s}^{-1}$.

Using the proper motion of the relativistic jets emitted from the system, we are also able to connect the distance and inclination angle (assumed to be perpendicular to the jet axis) for an assumed intrinsic speed of the jet. In 2002, bright radio knots are observed from GX 339–4 at the state transition and the head of one knot moved 12 arcsec in approximately 300 days (Gallo et al. 2004). From this

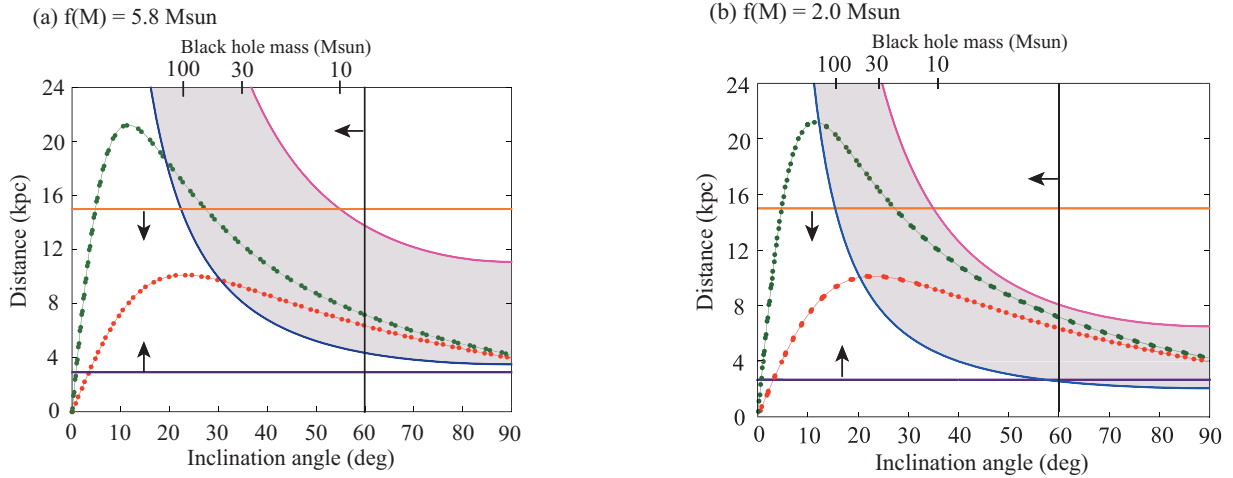


Fig. 1. Relation of the inclination angle, black hole mass, and distance of GX 339–4. The abscissa represents the inclination angle (bottom) and black hole mass (top). The mass function is assumed to be $5.8 M_{\odot}$ in the left panel and $2.0 M_{\odot}$ in the right panel. The orange horizontal line shows the upper limit of distance (15 kpc) derived from the velocity dispersions (Hynes et al. 2004), and the purple line corresponds the lower limit (3 kpc) determined with the extinction study (Zdziarski et al. 1998). The vertical line at $i = 60^{\circ}$ shows the upper limit of the orbital inclination angle by the absence of eclipse (Cowley et al. 2002). The relation between the inclination angle and distance, calculated from the 0.5–200 keV flux of GX 339–4 in very high state (Yamada et al. 2009) is presented by assuming $L/L_{\text{Edd}} = 1$ (pink, upper curve) and 0.1 (dark blue, lower curve), with the area for $0.1 \leq L/L_{\text{Edd}} \leq 1$ filled in gray. The red and green dotted lines show the relation between the inclination and distance derived from the jet motion observed by Gallo et al. (2004), where the intrinsic velocity is assumed to be $0.92c$ and $0.98c$, respectively.

apparent velocity, we derive the relation between the inclination angle and distance, assuming the intrinsic speed of the jet to be $0.98c$ (Fender et al. 1999b) or $0.92c$ (Mirabel & Rodríguez 1994), a typical value observed from the microquasar GRS 1915+105.

Also, recent work sets the lower limit of the companion-star mass, $M_C \geq 0.166M_{\odot}$, by considering the mass transfer process of low mass X-ray binaries (Muñoz-Darias et al. 2008). This minimum mass makes a tight constraint on the binary inclination, $i > 45$, by assuming that the black hole mass is less than $15M_{\odot}$, which is the largest mass ever known among Galactic BHBs (discussed in Kolehmainen & Done 2010). This is quite consistent with the constraints summarized in Figure 1 for both cases of the two $f(M_{\text{BH}})$ values.

3. X-Ray Observations and Data Reduction

3.1. Observations

We performed three sequential ToO (Target of Opportunity) observations of GX 339–4 with Suzaku (Mitsuda et al. 2007) on 2009 March 18, 25–26, and 30–31 (hereafter Epoch-1, -2, and -3, respectively), each for a net exposure of ~ 40 ksec. The ToO observations were triggered after the increase of the X-ray flux detected by RXTE/PCA scanning observations in 2009 February (Markwardt et al. 2009) and by Swift/BAT monitoring in March (Still et al. 2009), based on our approved Suzaku AO-3 program.

In Figure 2 we show the Suzaku hard-state observations in the context of the large data archive for GX339–4 produced with the RXTE PCA Instrument. We extracted the normalized PCA count rates in four energy bands, as

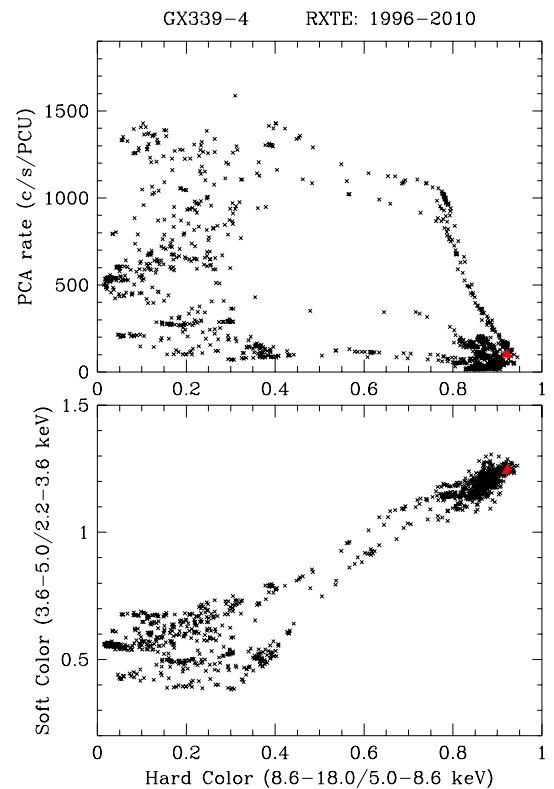


Fig. 2. Hardness-intensity diagram (upper) and color-color diagram (lower) of GX 339–4, obtained with RXTE/PCA during 1996–2010. The four orbits during our Suzaku campaign is highlighted in red (filled triangle), one point on MJD 54914 and three on MJD 54916.

Table 1. Summary of the Suzaku observations

Label	Observation Date (UT)		Observation ID	Net Exposure (ksec)		
	Start	End		XIS-0 and -3*	XIS-1†	HXD
Epoch-1	2009 March 18 01:53:13	2009 March 18 23:04:19	403011010	21.4	3.9	35.4
Epoch-2	2009 March 25 08:14:00	2009 March 26 06:30:24	403011020	19.4	3.6	34.8
Epoch-3	2009 March 30 11:27:27	2009 March 31 12:31:10	403011030	19.6	3.6	35.1

* XIS-0 and -3 were operated in the 1/4 window mode with 0.5 sec burst option.

† XIS-1 was in the full window mode with 0.5 sec burst option.

described by Lin et al. (2007), to construct the hardness-intensity diagram (HID; top panel) and color-color diagram (bottom panel). Each of the 1159 plotted points represents an interval of continuous exposure, with an average exposure time of 2.0 ks. These data have been filtered to eliminate exposures obtained when the source flux is fainter than $12.5 \text{ count sec}^{-1} \text{ PCU}^{-1}$ (or 5 mCrab at 2–30 keV), so that the statistical error bars remain similar to or smaller than the size of the plot symbols.

Four of these RXTE exposures overlap with the Suzaku observations (one on MJD 54914 and three on 54916), and the results for those data are plotted as red triangles. The HID in Figure 2 extends the results shown by Remillard & McClintock (2006), Figure 9d to cover RXTE observations through 2010 July 8. In the earlier work, the HID points are symbol-coded to show state assignments based on quantitative definitions, and observations in the hard state completely surround the regions occupied by the red points (i.e., the Suzaku-associated exposures) shown in Figure 2.

The Suzaku observations of GX 339–4 were conducted by using the X-ray Imaging Spectrometers (XISs) and the Hard X-ray Detector (HXD) at the HXD nominal position. The XISs are composed of three frontside-illuminated (FI) CCDs (XIS-0, -2 and -3) and a backside-illuminated (BI) CCD (XIS-1) covering the energy range of 0.2–12 keV. The BI-CCD has larger effective area than FI-CCDs below $\approx 1.5 \text{ keV}$ and is more sensitive to low energy photons. The HXD consists of silicon PIN diodes and GSO crystal scintillators, and is sensitive to hard X-ray photons in 10–70 keV and 40–600 keV bands, respectively. In our observations, the editing mode of the FI-CCDs was 2×2 and that of the BI-CCD was 3×3 . To reduce photon pile-up, XIS-0 and XIS-3 were operated with the 1/4 window and 0.5 sec burst option, and XIS-1 was used with the full window and 0.5 sec burst option. XIS-2 was not usable then because of the trouble of the instrument on 2006 November 9. The summary of the observations is given in Table 1.

3.2. Data Reduction

We utilized data products of both instruments reduced through Suzaku pipeline processing version 2.3.12.25. To extract light curves and spectra, the data were analyzed with HEASoft version 6.6.3 and the calibration data files (CALDB) released on 2009 October 7. Because the Suzaku attitude was still unstable shortly after the maneuver to the target, the data acquired in the first 2 ksec in Epoch-1 were discarded to avoid difficulties of analysis.

We analyzed the XIS cleaned event files in the “sky coordinates” system, where the small attitude variation of the spacecraft during the orbit is corrected. We extracted the counts of the FI-CCDs (XIS-0 and -3) and the BI-CCD (XIS-1) from circular regions centered on the target with the radii of $1.9'$ and $3.7'$, respectively. The regions enclose $\sim 90\%$ of the available photons in each field of view, whose area is a factor of 4 smaller in FI-CCDs than in BI-CCD because of the window option. The background of the XIS were taken from a source-free area with the same radii as the target. For the HXD, we used the modeled background files produced by the Suzaku HXD team¹. The PIN background, composed of the non X-ray background (NXB) and the cosmic X-ray background (CXB), was subtracted from the source spectra. Although there is additional background contribution from the Galactic ridge emission, the effect is estimated to be negligible ($\approx 0.5\%$ of the target flux) in our PIN data. For the background of GSO, only the NXB component was considered because the contribution of the CXB to the total background rate is less than 0.1% ².

The light curves of GX 339–4 in four energy bands, 0.7–2 keV, 2–10 keV, 14–50 keV, and 50–200 keV are plotted in Figure 3 for the three epochs. The PIN and GSO light curves were corrected for dead time, and the NXB was subtracted. Background subtraction was also performed for the XIS data. As presented in Figure 3, the count rates of the target in these energy bands exhibit a similar behavior to one another, suggesting that the overall spectral shape is mostly constant.

Figure 4 shows the time-averaged spectra of the XIS and the HXD in the three observations. To improve statistics, XIS-0 and -3 were combined each other. We created the response matrix files and auxiliary response files of the XIS with the FTOOLS `xisrmfgen` and `xissimarfgen`, respectively. As the response files of the HXD, we used `ae_hxd_pinhxnome5_20080716.rsp` for PIN, and `ae_hxd_gsohxnom_20080129.rsp` and `ae_hxd_gsohxnom_crab_20070502.arf`³ for GSO. To include possible uncertainties associated with the calibration of the instruments, 1% systematic error is introduced for each spectral bin of the XIS and the HXD.

To examine possible effects of pile-up in the XIS data, which should be more significant in the core region of the point spread function of the X-ray telescope, we also make

¹ <http://www.astro.isas.jaxa.jp/suzaku/analysis/hxd/pinnxb, gsonxb>

² <http://www.astro.isas.ac.jp/suzaku/analysis/hxd/gsonxb/>

³ <http://www.astro.isas.jaxa.jp/suzaku/analysis/hxd/gsoarf/>

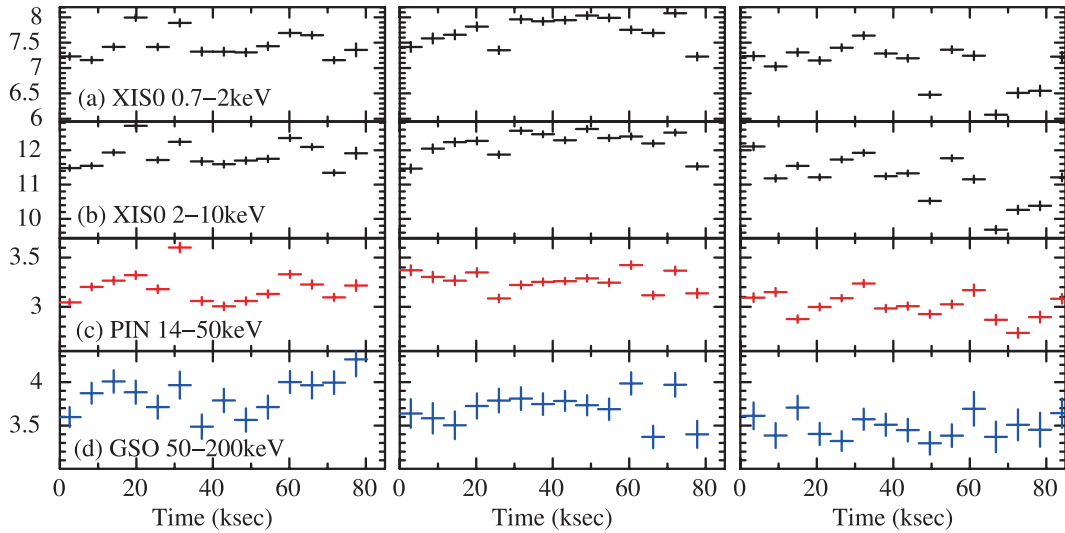


Fig. 3. X-ray light curves of GX 339-4 binned in 5760 sec. The ordinates represent the count rate (counts sec^{-1}) in the energy range of (a) XIS-0 0.7-2 keV, (b) XIS-0 2-10 keV, (c) PIN 14-50 keV, and (d) GSO 50-200 keV. The left, middle, and right panels present the results of Epoch-1, -2, and -3, respectively. The background subtraction (for the XIS and HXD) and dead time correction (for the HXD) are applied.

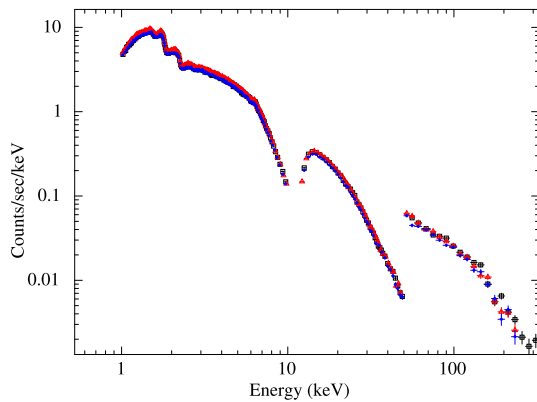


Fig. 4. Time-averaged Suzaku spectra obtained in Epoch-1 (black, open square), -2 (red, open triangle) and -3 (blue, filled circle). For clarity the XIS-1 data are not plotted.

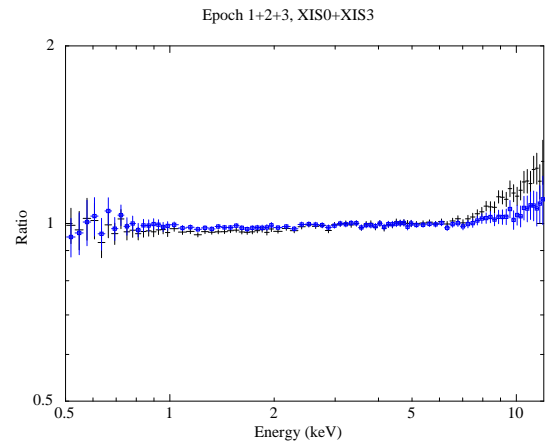


Fig. 6. Ratios of the XIS-0+XIS-3 spectra (sum of Epochs 1, 2, and 3) extracted from the whole circular region ($r < 1.9'$, black) and annulus of $r = 0.57' - 1.9'$ (blue, open square), divided by that from the $r = 0.95' - 1.9'$ annulus. They are normalized to be unity at 5.0 keV.

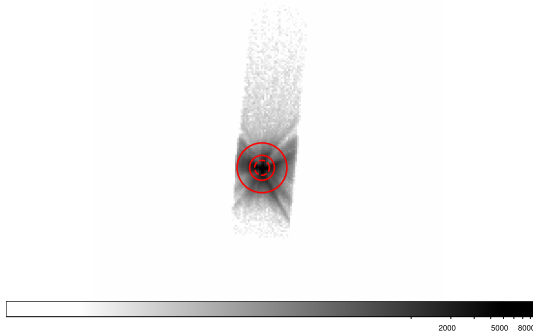


Fig. 5. XIS-0 image of Epoch-1 in the sky coordinates. The circles (red) correspond to radii of $1.9'$, $0.95'$, and $0.57'$ (dashed), which define the annulus regions used to check the pile-up effects.

the spectra of XIS-0 and XIS-3 in two annuli whose inner radii are set to be 30% ($0.57'$) and 50% ($0.95'$) of the outer radius ($1.9'$). The regions are illustrated in Figure 5 for XIS-0. For each annulus region, both XIS-0 and XIS-3 spectra in the three epochs are combined into a single one. Figure 6 plots the ratios of the spectra extracted from the whole circular region ($r < 1.9'$, black) and the $r = 0.57' - 1.9'$ annulus (blue), divided by that from the $r = 0.95' - 1.9'$ annulus, which can be regarded as free from pile-up. As noticed from the figure, the spectral ratio for the whole circular region shows a significant excess above ~ 8 keV attributable to pile-up. Thus, while we adopt the $r < 1.9'$ spectra to achieve the best statistics, the energy range above 8 keV is not utilized in our spectral analysis.

The difference from the $r = 0.95' - 1.9'$ spectrum is very small below this energy band, and we confirm that our results on the innermost disk radius derived from the iron-K profile (Section 4.3) are not affected by pile-up. We find that its estimate from the continuum fit (Section 4.2) could be affected by $\sim 20\%$ in Epoch 1 and by $< 10\%$ in Epochs 2 and 3, but this uncertainty does not change our conclusion on the black hole mass presented in Section 4.3.

4. Analysis of the Time-Averaged Suzaku Spectra

In this section, we present the analysis of the Suzaku spectra extracted above. The spectral fit is performed by using XSPEC version 11.3.2ag. In all spectral models, we assume solar abundances given by Anders & Grevesse (1989). We employ the `wabs` model for Galactic interstellar absorption, whose column density is set to be a free parameter. The quoted errors refer to 90% confidence levels for a single parameter.

4.1. Broad Band Fitting

To best constrain the origin of the X-ray emission, the broad-band spectra of the XIS and HXD are simultaneously analyzed. We use the data in the energy range of 0.5–8.0 keV for XIS-1, 1.0–8.0 keV for XIS-0 plus -3, 15–50 keV for PIN, and 50–310 keV for GSO. To avoid the calibration uncertainties around the instrumental Si-K and Au-M edges in the responses, the spectra in the 1.7–1.9 keV and 2.1–2.3 keV energy band are excluded in the fit. The cross normalization between HXD and XIS-0+XIS-3 spectra is fixed at 1.18 based on the calibration result using the Crab Nebula data⁴, while that between XIS-1 and XIS-0+XIS-3 is set free.

As shown in Figure 4, the spectra of the three observations exhibit similar shape to one another, indicating that the physical state of the source remain the same in the three epochs. We find that the overall continuum in the 2–100 keV band can be roughly approximated by a power law of a photon index of ~ 1.5 in each epoch. This confirms that GX 339–4 was the low/hard state throughout our observations.

Following the previous studies of BHBs in the low/hard state with Suzaku, we adopt a model from a standard accretion disk and its thermal Comptonization by a hot corona as the basic description of the broad band continuum. The disk emission is assumed to be the multi-color blackbody radiation modeled by `diskbb` (Mitsuda et al. 1984). For the Comptonization component, we employ the `compPS` model (Poutanen & Svensson 1996), where the Comptonized spectrum is computed from the electron temperature, the optical depth of scattering, and the energy distribution of incident photons. We consider only thermal electrons by setting `gmin` = -1 . We assume that the Comptonization cloud is spherical (i.e., `geom` = 4) and that seed photons are entirely originated in the standard disk ($T_{\text{bb}} = -T_{\text{in}}$ in the XSPEC terminology).

The `compPS` code is able to take into account a reflection component from the disk as calculated by Magdziarz & Zdziarski (1995). Its parameters are the solid angle

of the reflector visible from the source ($\Omega/2\pi$), ionization parameter (ξ), inclination angle (i), and temperature, which we fix at 10^6 K. This component is further relativistically blurred with the `diskline` profile (Fabian et al. 1989), by assuming a radial dependence of emissivity as $\propto R^\beta$ between the inner and outer disk radius (R_{in} and R_{out}). We fix $R_{\text{in}} = 10R_g$, $R_{\text{out}} = 10000R_g$, $i = 50^\circ$, and $\beta = -2.3$, based on the results from the analysis of the XIS spectra in the 3–8 keV band (Section 4.3). Although Compton broadening is not taken into account in the reflection model, the effect is negligible in our case because the ionization parameter is found to be very low ($\xi \lesssim 2$, Section 4.1) and estimated temperature does not exceed $\sim 10^6$ K as assumed. The iron K fluorescent line at ~ 6.4 keV is simply fitted with a Gaussian at this stage, whose detailed modeling does not affect the analysis of the broad band continuum. Combining all the components described above, the model is expressed as `wabs × (compPS + diskbb + gauss)` on the XSPEC terminology.

As the first trial, we perform a spectral fit without reflection components. The result is far from acceptable, yielding $\chi^2/\nu = 1219/950$ (Epoch-1), 1160/907 (Epoch-2), and 1195/873 (Epoch-3), with residuals shown in the second panels of Figure 7. As noticed, there remains an absorption edge-like feature above ~ 7 keV in the XIS spectra and a hump structure at ~ 30 keV in the PIN data. They are strong evidence for the reflection component, as reported in previous broad band observations of GX 339–4 in the same state (e.g., Ueda et al. 1994).

We find that inclusion of the reflection component in the model greatly improve the fit, although the fit goodness is not yet satisfactory, $\chi^2/\nu = 1161/948$, 1083/905, and 1136/871 for Epoch-1, -2, and -3, respectively. There is still a discrepancy between the data and model in the 15–50 keV region, as shown in the third panels of Figure 7. We confirm that this is not caused by any systematic uncertainties in the response or background of PIN, based on the calibration using the Crab Nebula and comparison of the background model with the dark-Earth occultation data in our observations. Similar residuals are also found from other BHBs in the low/hard state when fitted with the same model (GRO J1655–40 by Takahashi et al. 2008 and Cyg X-1 by Makishima et al. 2008). A possible reason for the discrepancy is that the corona cannot be described by a constant temperature and optical depth, and therefore we add another `compPS` component. This "double `compPS`" model was successfully applied to the low/hard state spectra of BHBs, such as Cyg X-1 (Makishima et al. 2008; Gierliński et al. 1997) and GRO J1655–40 (Takahashi et al. 2008). We tie all the parameters of the additional `compPS` component to those of the other `compPS` component except for the optical depth τ and normalization.

The best-fit model and residuals of fit using the double `compPS` model are displayed in the top and bottom panels of Figure 7, respectively. In Figure 8, the best-fit model spectrum in the νF_ν form (where F_ν is the energy flux) is plotted, with contribution of each component,

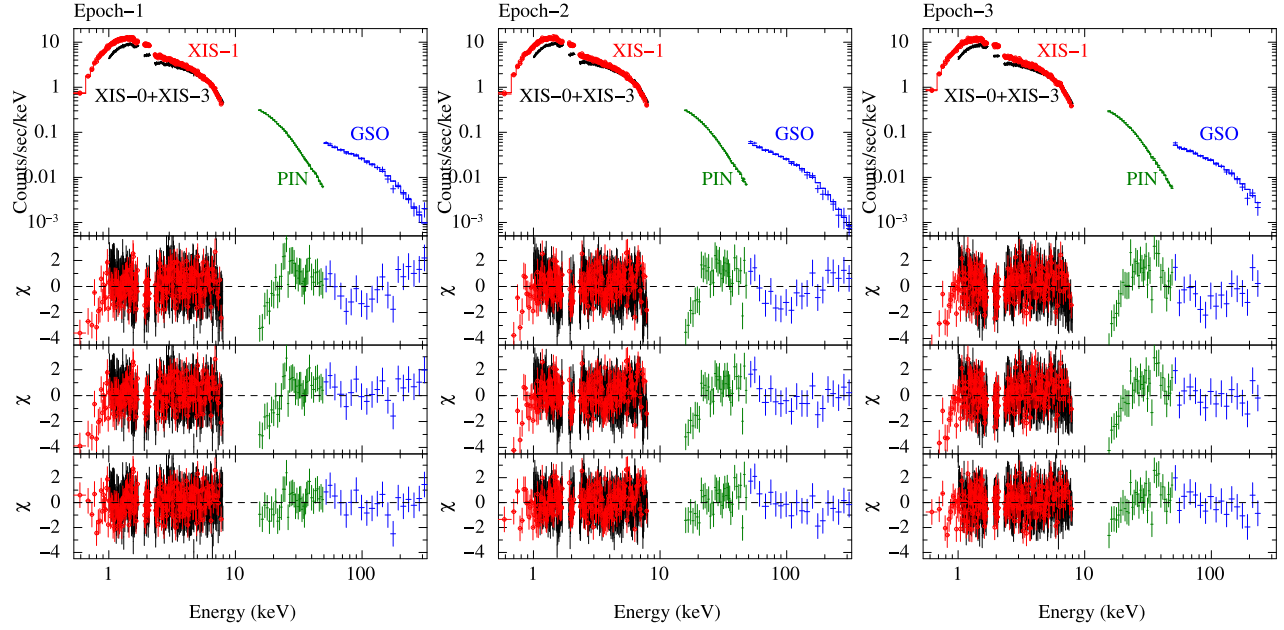


Fig. 7. Simultaneous fit to the XIS-1 (red, open circle), XIS-0+XIS-3 (black), PIN (green), and GSO (blue) spectra with the double compPS model in Epoch-1, -2, and -3. The second, third, and bottom panels show the residuals of the fit with the single compPS model without reflection, that with reflection, and the double compPS model with reflection, respectively.

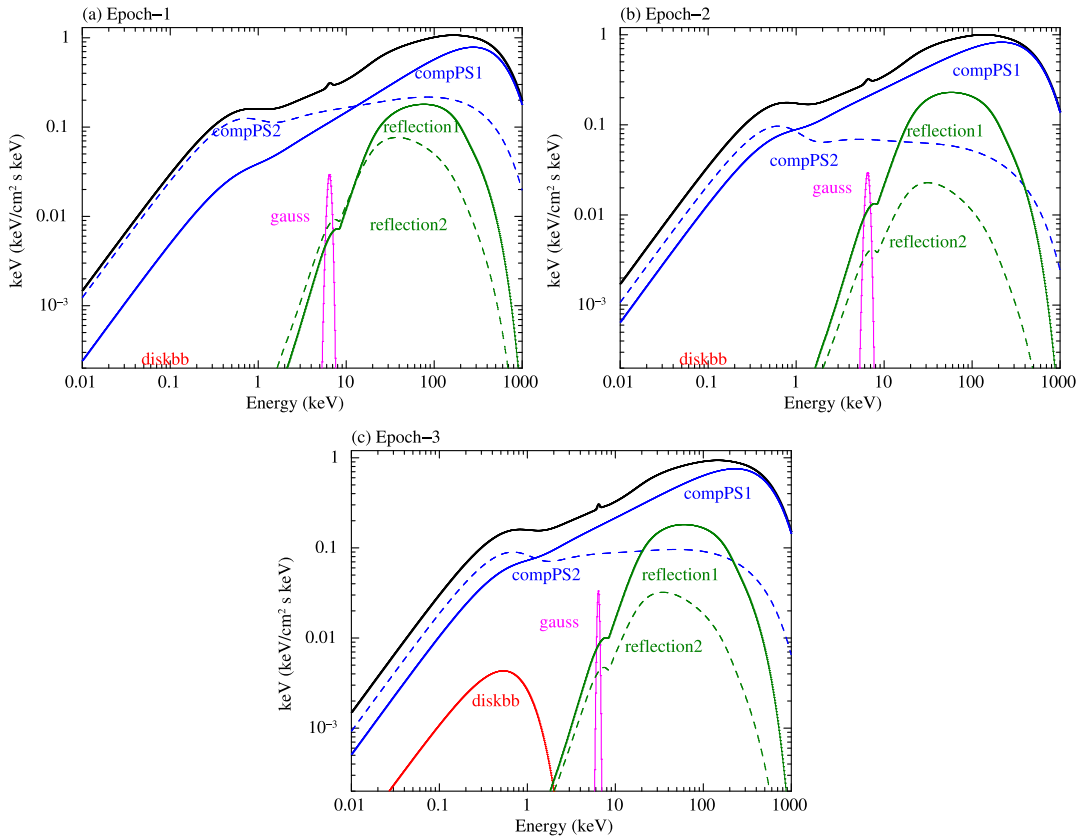


Fig. 8. The best-fit double compPS model of each epoch in the νF_ν form, corrected for the interstellar absorption. Each component is separately plotted.

Table 2. Parameters of the Double Compton Model* for Epoch-1, -2, and -3

Component	Parameter	Epoch-1	Epoch-2	Epoch-3
wabs	N_{H} (10^{21}cm^{-2})	5.35 ± 0.03	$5.52^{+0.05}_{-0.03}$	5.46 ± 0.03
diskbb	T_{in} (keV)	0.223 ± 0.003	$0.220^{+0.002}_{-0.02}$	$0.225^{+0.002}_{-0.003}$
	normalization [§]	<120	<255	250^{+120}_{-110}
	photon flux	1.59×10^{-3}	1.51×10^{-3}	4.09×10^{-2}
compPS [†] (harder component)	T_{e} (keV)	176^{+4}_{-6}	171^{+6}_{-5}	177^{+5}_{-6}
	(y-parameter [#])	$1.55^{+0.04}_{-0.01}$	1.2 ± 0.4	$1.24^{+0.17}_{-0.01}$
	τ	$1.12^{+0.07}_{-0.03}$	0.9 ± 0.3	$0.90^{+0.04}_{-0.03}$
	photon flux	0.283	0.679	0.547
compPS [†] (softer component)	(y-parameter [#])	0.63 ± 0.01	0.40 ± 0.02	$0.51^{+0.02}_{-0.01}$
	τ	0.46 ± 0.02	$0.30^{+0.02}_{-0.01}$	0.37 ± 0.02
	photon flux	1.10	0.889	0.798
reflection [‡]	ξ (erg cm s^{-1})	$0.474^{+1.561}_{-0.470}$	< 1.71	$0.481^{+1.767}_{-0.477}$
	$\Omega/(2\pi)$	0.46 ± 0.01	$0.48^{+0.02}_{-0.01}$	$0.43^{+0.02}_{-0.01}$
Gaussian	E_{cen} (keV)	$6.41^{+0.04}_{-0.06}$	6.44 ± 0.06	$6.40^{+0.04}_{-0.03}$
	EW (eV)	96^{+9}_{-11}	99^{+10}_{-13}	58^{+7}_{-8}
	σ (keV)	$0.35^{+0.10}_{-0.03}$	$0.38^{+0.11}_{-0.06}$	$0.18^{+0.04}_{-0.03}$
	$R_{\text{in}}^{\text{cont}}$ (km)**	117 ± 2	128^{+22}_{-2}	115 ± 2
Unabsorbed flux	$\chi^2/\text{d.o.f.}$	996/946	873/903	940/869
	0.5–2 keV ($\text{erg cm}^{-2} \text{s}^{-1}$)	3.5×10^{-10}	3.8×10^{-10}	3.5×10^{-10}
	2–10 keV ($\text{erg cm}^{-2} \text{s}^{-1}$)	6.4×10^{-10}	6.6×10^{-10}	6.2×10^{-10}
	10–300 keV ($\text{erg cm}^{-2} \text{s}^{-1}$)	4.4×10^{-9}	4.3×10^{-9}	4.0×10^{-9}

Notes. The errors are 90% confidence level for a single parameter.

* The model is expressed as **wabs** \times (**compPS** + **compPS** + **diskbb** + **gauss**).

† We set $g_{\text{min}} = -1$ (thermal electrons only) and $geom = 4$ (spherical geometry). The seed photons for Comptonization is the MCD emission from the disk (i.e., T_{bb} in **compPS** is linked as $-T_{\text{in}}$ in **diskbb**).

‡ We assume the solar abundances for iron and heavy elements. The temperature of the reflector is fixed at 10^6 K. The reflection parameters of the two **compPS** components are linked each other, with R_{in} , R_{out} , β , and i fixed at the best-fit values from the iron-K line fit summarized in Table 3.

§ $((r_{\text{in}}/\text{km})/(D/10\text{kpc}))^2 \cos \theta$, where r_{in} and θ are the inner disk radius and the disk inclination, respectively.

|| Unabsorbed photon flux in units of photons $\text{cm}^{-2} \text{s}^{-1}$ in the 0.01–100 keV band based on the best-fit parameters.

Compton y-parameter calculated as $4\tau kT_{\text{e}}/(m_e c^2)$.

** Estimated innermost disk radius derived from the flux of direct MCD and Comptonization components, assuming a distance of 8 kpc and an inclination of 50° . Those have been corrected for the inner boundary condition and color/effective temperature ratio (see Section 4.2).

corrected for the interstellar absorption. The best-fit values are summarized in Table 2. The fit is significantly improved, $\chi^2/\nu = 996/946$, $873/903$, $940/869$, compared with the single **compPS** model, yielding F-test probabilities of 4×10^{-32} , 7×10^{-43} , and 1×10^{-36} for Epoch-1, -2, and -3, respectively. We find that the contribution of the direct MCD component (**diskbb**) is very small ($< 2\%$ in flux at 0.5 keV), and only its upper limit is obtained in Epochs 1 and 2. The absorption column density is determined as $N_{\text{H}} \approx 5.4 \times 10^{21} \text{ cm}^{-2}$, which is consistent with previous works by Méndez & van der Klis (1997) and Kong et al. (2000).

4.2. Estimate of the Innermost Disk Radius

Assuming that the number of photons emitted from the disk is conserved in the Comptonization process, we can estimate the innermost radius of the disk from the following equation (Kubota & Makishima 2004),

$$F_{\text{disk}}^p + F_{\text{thc}}^p 2 \cos i = 0.0165 \left[\frac{r_{\text{in}}^2 \cos i}{(D/10 \text{ kpc})^2} \right] \left(\frac{T_{\text{in}}}{1 \text{ keV}} \right)^3$$

$$\text{photons s}^{-1} \text{ cm}^{-2}. \quad (2)$$

where F_{disk}^p and F_{thc}^p are the unabsorbed 0.01–100 keV photon flux from the disk and thermal Compton component, respectively. Here it is assumed that the Comptonized emission is isotropic and there are few photons that are scattered back to the disk. Table 2 list the values of F_{disk}^p and F_{thc}^p (for the two Comptonization components) in each epoch; the direct disk flux is found to be less than 3% of the total Comptonized one. Assuming $i = 50^\circ$ (Section 4.2), we derive the innermost disk radius for Epoch-1, -2 and -3 to be $r_{\text{in}} = (98 \pm 2)D_8$, $(107^{+19}_{-2})D_8$, $(97 \pm 2)D_8$ km, respectively, where D_8 is the distance to GX 339–4 in the unit of 8 kpc. Here the errors reflect the uncertainties in T_{in} . Multiplying this radius by the correction factor, 1.19, for the boundary condition and ratio of the color/effective temperature of the multi-color disk (see Kubota et al. 1998), yields an actual innermost radius of $R_{\text{in}}^{\text{cont}} = (117 \pm 2)D_8$, $(128^{+22}_{-2})D_8$, $(115 \pm 2)D_8$ km for the three epochs.

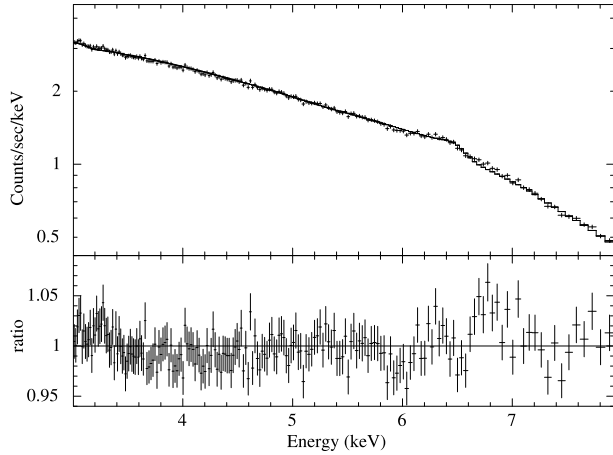


Fig. 9. Iron K-line fit to the 3–8 keV XIS-0+XIS-3 spectra in 2009 March with the `diskline` model for a fixed emissivity index of $\beta = -3$. The ratio between the data and best-fit model are shown in the lower panel.

4.3. Iron-K Line Fitting

To best constrain the disk geometry from the iron-K emission line profile, we fit the XIS spectra in the 3–8 keV band with the relativistic disk line model `diskline` (Fabian et al. 1989) with the reflection continuum self-consistently. Here we consider both $K\alpha$ and $K\beta$ lines; although the contribution of the $K\beta$ line is generally weak and has been neglected in most of previous work, we find that it affects the final results. Since the parameters can be only weakly constrained from the spectra in each epoch due to the limited photon statistics, we combined the spectra of the three epochs separately for XIS-0+XIS-3 and for XIS-1 to discuss the time-averaged properties over the three observations. This is justified because the continuum fit to the individual broad band spectra gives similar (if not the same) results to one another, and the estimated inner disk radii ($R_{\text{in}}^{\text{cont}}$) stay constant within 10% level as shown in the previous subsection, which is much smaller than the statistical error we will obtain from the line profile analysis. As a continuum, we adopt the results from double `compPS` fit using the broad-band XIS+HXD spectra averaged over the three epochs, and replace the `gauss` model with `diskline` for the iron line. In the fit of the XIS spectra, the normalization and optical depth of the hard Comptonization component, the most dominant one in the 3–8 keV band, are treated as free parameters. Since the continuum shape is hard to constrain within the limited band coverage, they are allowed to float only within their 90% errors obtained in the XIS+HXD fit, and the other continuum parameters are fixed at the best-fit values.

The `diskline` model has five parameters, the inner and outer disk radius (R_{in} and R_{out}), inclination angle (i), power law index of emissivity β , and intrinsic line center energy (E_{cen}). We fix $R_{\text{out}} = 10000R_g$, which is difficult to constrain from the data. The line center energies are fixed at 6.40 keV ($K\alpha$) and 7.06 keV ($K\beta$) to make them consistent with the low ionization parameter obtained from

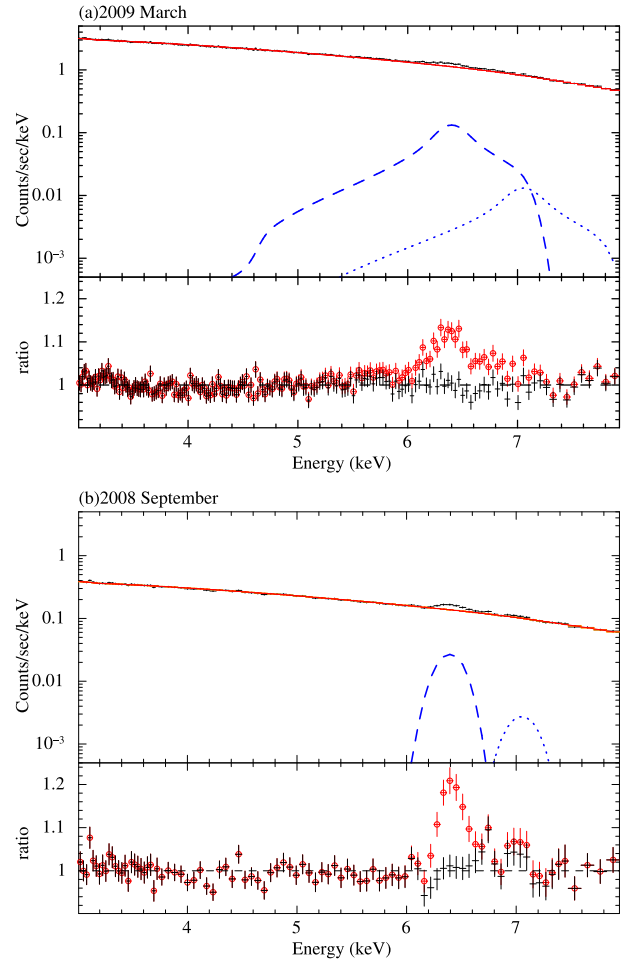


Fig. 10. Fitting results of the 3–8 keV XIS-0+XIS-3 spectra with the `diskline` model, obtained from the observations in 2009 March (our data, brighter state) and that in 2008 September (Tomsick et al. 2009). The top panel plots the data (black, with error bars) and the best-fit models of the iron- $K\alpha$ (blue, dashed) and - $K\beta$ lines (blue, dotted) and of the continuum (red, solid). The ratio between the data and best-fit model are shown in the lower panels for the 2009 and 2008 data, respectively; the red ones (open circles) correspond to the case when the iron-K line is excluded from the model. For clarity the XIS-1 data are not plotted.

Table 3. Parameters of the Iron-K Line Fit*

Component	Parameter	Value
diskline ($K\alpha$)	E_{cen} (keV)	6.4 (fixed)
	EW (eV)	87^{+10}_{-11}
diskline ($K\beta$)	E_{cen} (keV)	7.06 (fixed)
	Emissivity law β	-2.3 ± 0.1
	i (deg)	46 ± 8
	R_{in} (R_g)	$13.3^{+6.4}_{-6.0}$
	intensity ratio ($K\beta/K\alpha$)	0.13 (fixed)
	$\chi^2/\text{d.o.f.}$	273/271

Notes. The errors are 90% confidence level for a single parameter.

* The continuum model is `wabs` \times (`diskbb` + `compPS` + `compPS`).

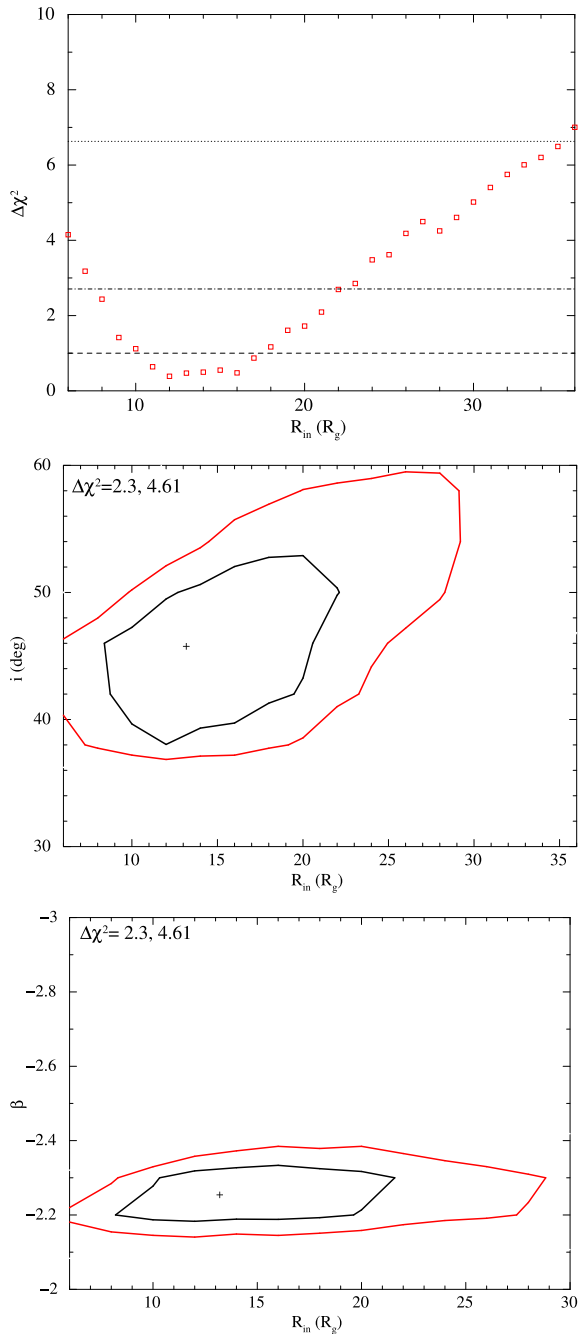


Fig. 11. *Top:* Delta chi-squared values plotted against R_{in} obtained from the `diskline` fit. The dashed, dash-dotted, and dotted lines represent 68%, 90%, and 99% confidence limits for a single parameter, respectively. *Middle:* Confidence contour between the inner radius R_{in} and inclination i at 90% (red, outer) and 68% (black, inner) confidence limits for two parameters. *Lower:* Confidence contour between the inner radius R_{in} and emissivity index β at 90% (red, outer) and 68% (black, inner) confidence limits for two parameters.

the reflection continuum. We also fix the intensity ratio between the $K\beta$ and $K\alpha$ at 0.13, a theoretical value for the iron K-fluorescence process (Kaastra & Mewe 1993). The rest are left as free parameters. Because the reflection continuum must also be blurred in the same manner as the emission line, we tie R_{in} , R_{out} , and β in the `diskline` model with those of the reflection component included in the `compPS` model. The result on the inclination can be compared with the independent constraints presented in Figure 1. When the emissivity index is fixed at $\beta = -3$, we find that the fit is not acceptable ($\chi^2/\text{d.o.f.} = 323/272$), showing a significant discrepancy between the data and model in both sides of the iron line (see Figure 9). In addition, the best-fit inclination angle for $\beta = -3$ is found to be $\approx 20^\circ$, which is not reasonable since the black hole mass exceeds $100M_\odot$ according to Figure 1, unless the inner accretion disk is heavily warped with respect to the binary plane. Thus, we vary β in the range $-3 \leq \beta \leq -2$ as a free parameter.

The result of the fit is plotted in Figure 10, and the best-fit parameters are listed in Table 3. We also show the increment of χ^2 in terms of R_{in} , and confidence contour between R_{in} and i , and that between R_{in} and β in Figures 11 (a), (b), and (c), respectively. The inclination angle now becomes $i = 46 \pm 8$ degrees, which is reasonable in terms of the black hole mass (Figure 1). The resulting inner radius is $R_{\text{in}} = 13.3^{+6.4}_{-6.0} R_g$, suggesting that the standard disk is extended close to the ISCO of a non-rotating black hole but is likely truncated at 90% confidence level (see Figure 11).

To compare with $R_{\text{in}}^{\text{cont}}$, the unit of the innermost disk radius derived through the iron-K line fit must be converted to km; $R_{\text{in}} = 13.3^{+6.4}_{-6.0} R_g$ corresponds to $R_{\text{in}} = 200^{+100}_{-90} M_{10}$ km, where M_{10} is the black hole mass in the unit of $10 M_\odot$. Thus, the results from the continuum and iron-K line profile analysis become consistent if the BH mass is the range of $(4\text{--}16)M_\odot$, assuming the distance of 8 kpc.

4.4. Comparison with 2008 Suzaku data

Tomsick et al. (2009) observed GX 339-4 in the fainter low/hard state using Suzaku, from 2008 September 24 22:37:25 to 27 02:19:24 (UT) with a net exposure of 100 ksec for the XIS and 80 ksec for the HXD (ObsID: 403067010). The 1–100 keV flux of the source was 2.4×10^{-10} erg cm $^{-2}$ sec $^{-1}$ in this period, which is approximately 14 times smaller than that of our 2009 data. As described in Section 4.1, the best-fit R_{in} value in the 2009 data is $R_{\text{in}} = 13.3^{+6.4}_{-6.0}$, apparently a factor of >8 smaller than the 2008 result by Tomsick et al. (2009). We note, however, that the derived R_{in} is coupled with both inclination and emissivity index. To eliminate the uncertainties, we re-analyze the data of the 2008 observation. The data reduction is made according to the standard procedure from the cleaned event files of processing version 2.2.11.22. We extract the XIS time-averaged spectra in the 0.5–10.0 keV band. The XIS-0 and XIS-3 spectra are co-added together with their responses.

We analyze the spectra with the model composed of an

Table 4. Parameters of the Iron-K Line Fit to the Tomsick et al. (2009) Data*

Component	Parameter	Value
diskline ($K\alpha$)	E_{cen} (keV)	6.4 (fixed)
	EW (eV)	77^{+18}_{-13}
diskline ($K\beta$)	E_{cen} (keV)	7.06 (fixed)
	Emissivity law β	-2.3 (fixed)
	i (deg)	50 (fixed)
	R_{in} (R_g)	190^{+710}_{-90}
	intensity ratio ($K\beta/K\alpha$)	0.13 (fixed)
	$\chi^2/\text{d.o.f.}$	444/402

Notes. The errors are 90% confidence level for a single parameter.

* The continuum model is `wabs × powerlaw`.

absorbed power law plus two iron line (diskline) components for $K\alpha$ and $K\beta$ line. For the analysis, we use the XIS-0+XIS-3 and XIS-1 spectra in the 3–8 keV range. We fix the inclination angle at $i = 50^\circ$ and the emissivity index at $\beta = -2.3$ according to our results of the Suzaku 2009 data. The quality of the fit is found to be acceptable, $\chi^2/\nu = 444/402$, with the best-fit photon index of $\Gamma = 1.61 \pm 0.01$ and column density of $N_{\text{H}} = 5.31 \pm 0.07 \times 10^{21}$. The XIS spectra, best-fit model, and their ratio are plotted in Figure 10. Table 4 summarizes the best-fit parameters. It is seen that the iron-K lines in the 2008 data is significantly narrower than those observed in 2009. The resulting inner disk radius is found to be $R_{\text{in}} = 190^{+710}_{-90}$, which is ≈ 14 times larger (at least 5 times larger within the statistical errors) than that in our observations.

5. Near-Infrared Observations and Data Analysis

We carried out near-infrared photometric observations of GX 339–4 on 11 nights over a period from 2009 Feb 27 to 2009 March 23, using the SIRIUS camera (Nagayama et al. 2003) on the 1.4 m IRSF telescope at the South African Astronomical Observatory (SAAO). SIRIUS is a JHK_s -simultaneous imaging camera, which has three 1024×1024 HAWAII arrays and covers a field of view of $7'.7 \times 7'.7$ with a scale of $0''.45 \text{ pixel}^{-1}$. The log of observations is given in Table 5. The typical seeing (FWHM) during the observations was $\sim 1''.4$ (3 pixels) in the J band.

After a standard data reduction procedure for near-infrared array images using the IRAF analysis package (dark subtraction, flat-field correction and sky subtraction), 10 dithered images were combined to reject bad pixels and improve the S/N ratio. Hence, each magnitude in Figure 12 was determined from 50 or 100 sec integration. Aperture photometry was made with an aperture of 12-pixel radii. Photometry with smaller apertures gave similar results. We used the 2MASS data of about 150 stars in the field for magnitude calibration. The 1-day averaged magnitudes in the JHK_s band are listed in Table 5.

The J ($1.25 \mu\text{m}$) and K_s ($2.14 \mu\text{m}$) light curves with the $J - K_s$ color are plotted in Figure 12, together with those of Swift/BAT in the 15–50 keV band and RXTE/ASM in the 2–12 keV band. As noticed, the daily averaged

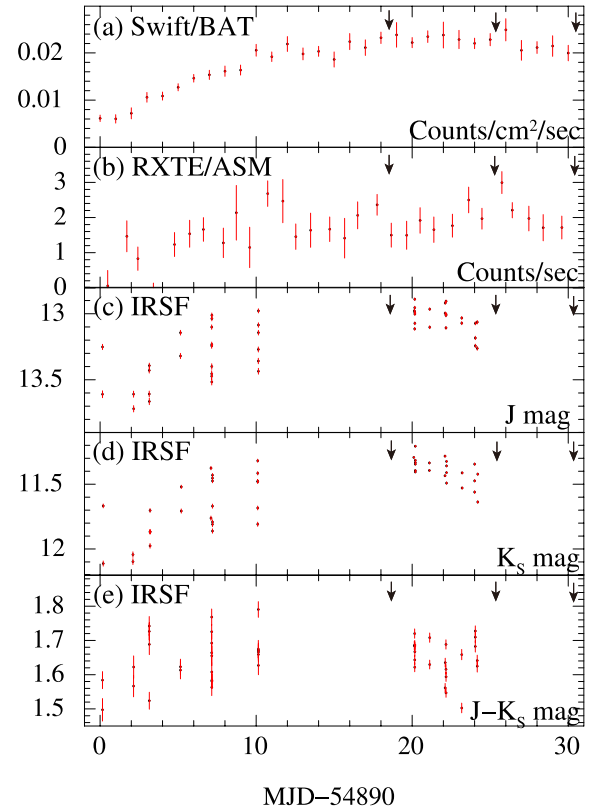


Fig. 12. X-ray (15–50 keV and 2–12 keV) and IR (J and K_s band) light curves and $J - K_s$ magnitudes of GX 339–4 obtained with Swift/BAT, RXTE/ASM, and IRSF/SIRIUS in 2009 March. The abscissa represents the date of MJD–54890, where 1 corresponds to 2009 March 1. The IR magnitudes are calibrated based on the Two Microns All Sky Survey (2MASS) Point Source Catalog, by using stars in the field of view. The arrows in each panel show the epochs of our Suzaku observations.

K_s band flux is correlated positively with the hard X-ray flux. Significant variation in the $J - K_s$ color by < 0.3 magnitudes is observed on time scale of 100 sec, although we find no clear correlation between the color and magnitude. The H ($1.63 \mu\text{m}$) band light curve is not plotted because they basically follow the same trend as the J and K_s light curves.

The left panel of Figure 13 shows the SED of GX 339–4 at the near-infrared to optical wavelengths in the νF_ν form. Utilizing the IRSF data taken between 2009 March 20 to 24, when the Swift/BAT flux was nearly constant around the Suzaku observation epoch, we plot the averaged photometry of the $J-H-K_s$ bands, the spectrum with the reddest $J - K_s$ color, and that with the bluest color. For comparison, the near infrared to optical data acquired in 1981 and 1997 in the low/hard state are also plotted (Corbel & Fender 2002, and references therein). In the right panel, a combined SED of GX 339–4 over the radio to X-ray bands is shown, although they are not simultaneous except for the IRSF and Suzaku data, which are quasi-simultaneous. The interstellar absorption is corrected in the X-ray spectrum, and all the near infrared

Table 5. The Log of Near-infrared Observations

Date*	Number of Observations†	Integration Time per Frame (sec)	Averaged Magnitude		
			<i>J</i>	<i>H</i>	<i>K_S</i>
Feb 28	2	5	13.43 ± 0.03	12.60 ± 0.02	11.89 ± 0.03
Mar 2	2	5	13.66 ± 0.03	12.80 ± 0.02	12.07 ± 0.03
Mar 3	4	5	13.52 ± 0.04	12.67 ± 0.03	11.85 ± 0.03
Mar 5	2	5	13.23 ± 0.03	12.40 ± 0.02	11.61 ± 0.02
Mar 7	9	5	13.27 ± 0.06	12.40 ± 0.04	11.63 ± 0.05
Mar 10	6	5	13.21 ± 0.05	12.30 ± 0.03	11.53 ± 0.03
Mar 20	7	10	13.00 ± 0.03	12.12 ± 0.02	11.33 ± 0.02
Mar 21	2	10	13.03 ± 0.02	12.16 ± 0.01	11.36 ± 0.01
Mar 22	6	10	12.99 ± 0.03	12.11 ± 0.02	11.38 ± 0.02
Mar 23	2	10	13.05 ± 0.02	12.17 ± 0.01	11.47 ± 0.01
Mar 24	5	10	13.16 ± 0.03	12.30 ± 0.02	11.49 ± 0.02

* All observations were made in 2009.

† We carried out 10 ditherings at each time.

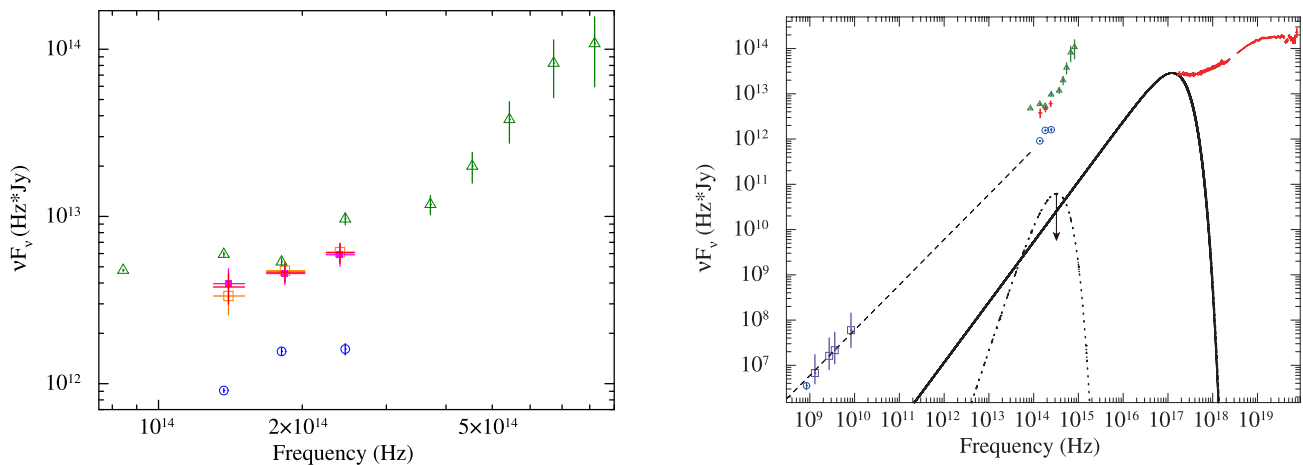


Fig. 13. Multiwavelength SED of GX 339-4 in the νF_ν form, corrected for the interstellar absorption/extinction. In the left panel, the data from our IRSF/SIRIUS observations, those obtained in 1981 and 1997 (Corbel & Fender 2002) are shown in red, green (open triangle), and blue (open circle), respectively. The IRSF fluxes averaged over MJD 54910–54915 are plotted in red, that with the reddest $J - K_s$ color are in pink (filled square), and with the bluest color in orange (open square). In the right panel, the Suzaku spectra and the radio data in 1992–1999 (Fender 2001) and 1997 (Corbel & Fender 2002) are displayed in red, purple (open square), and blue (open circle), respectively, in addition to the same data as the left panel (without the reddest/bluest $J - K_s$ data). The solid line shows the estimated contribution of intrinsic multicolor disk emission, including the Compton scattered photons. The dotted line represents the upper limit of the contribution from the companion star, assuming a blackbody with an effective temperature of 4000 K (Zdziarski et al. 2004). The dashed line shows a power law with an index of 1.0 ($\alpha = 0.0$), fitted to the Fender (2001) results, for illustrative purpose.

data are dereddened by assuming $A_V = 3.7$ (Corbel & Fender 2002). Both X-ray and infrared fluxes in our observations are between those obtained in 1981 and 1997, which differ by a factor of 4. By fitting the J - H - K_s spectra by a power law with $F_\nu \propto \nu^\alpha$, we obtain $\alpha = -0.10 \pm 0.08$ (average), which varied between $\alpha = -0.20 \pm 0.15$ (the reddest data) and $\alpha = +0.08 \pm 0.10$ (bluest).

6. Discussion

6.1. *Suzaku* Results and Inner Disk Structure

With *Suzaku*, we have obtained the best quality simultaneous, broad band X-ray spectra ever obtained from GX 339–4 in the low/hard state, covering the 0.5–310 keV band. We demonstrate that the spectra in the three observations can be well described by thermal Comptonization of disk photons dominating the flux of the entire band, a direct MCD component, and a reflection component with an iron-K emission line. The disk photon flux is very small ($\lesssim 3\%$ of the Comptonized one), indicating that the inner part of the optically thick disk is almost fully covered by the corona. The strength of the reflection component (in terms of the solid angle, $\Omega/2\pi \approx 0.45$) and the ionization parameter of the reflector ($\xi \lesssim 2$) are consistent with the result from a previous *Ginga* study in the similar intensity state (in 1989 September) analyzed with a power law continuum (Ueda et al. 1994), but are now determined with much smaller uncertainties thanks to the better energy resolution and wider coverage of *Suzaku*.

We find that in each epoch, two thermal Comptonization components (“double CompPS” model), with the same electron temperature ($T_e \approx 175$ keV) but different optical depths ($\tau \approx 0.4$ and 1), gives a reasonable description of the incident continuum spectrum. This indicates that the Comptonizing corona can be regarded isothermal but has a more complex geometry than that assumed in a single zone, spherical model. In fact, the corona may have a more disk-like geometry and/or inhomogeneous structure, where the optical depths of Comptonization as measured from the input source (i.e., the standard disk) is not spatially constant. Similar conclusions have been obtained from Cyg X-1 (Makishima et al. 2008) and GRO J1655–40 (Takahashi et al. 2008) in the low/hard state with *Suzaku*. Thus, we suggest that such physical conditions of the corona may be a common feature in the low/hard state of BHBs. Although the overall shape of the broad-band spectra of GX 339–4 look similar during our observations, the optical depths and relative fraction of the two Comptonization components are found to be slightly different among the three epochs while the electron temperature remains constant at ≈ 175 keV. This suggests that the geometry of the corona varies on time scale of several days in the low/hard state even at an almost same ($< 5\%$) luminosity level. We note that the double CompPS fit still leaves small, systematic discrepancies between the data and model in the PIN $\lesssim 30$ keV region. This is not surprising since the change of physical parameters of the corona should be continuous in reality, while the double CompPS model gives only

an approximation. Application of more complex (and realistic) Comptonization models is left as future work.

The analysis of the iron-K line profile has enabled us to tightly constrain the inclination angle and innermost radius of the optically thick disk. We obtain $i \sim 50$ degrees, which is converted to the black hole mass of 4–16 M_\odot for the allowed range of the mass function of this binary (see Section 2). The estimated mass range looks more reasonable than huge masses ($> 100 M_\odot$) calculated from $i = 18$ degrees, if the disk is not strongly warped, as claimed by Miller et al. (2006) and Reis et al. (2008) based on their detection of a broad iron-K line. The reason for this large discrepancy is unclear, but it should be noted that results on a very broad iron-K line often strongly depend on the continuum modeling and may be partially affected by pile-up of the CCD data (Yamada et al. 2009; Done & Diaz Trigo 2010).

The emissivity index obtained from the empirical diskline fit also carries important information for understanding the disk structure. In our state, a part of the iron-K line emitted from the innermost radii should be subject to Comptonization as well, under the situation that the hot corona almost fully covers the inner disk. This causes significant broadening of the scattered line component, with an averaged fractional energy gain of $\Delta E/E \sim 4kT_e/mc^2 \sim 1$, which makes it almost undetectable as a line. This would partially explain the observed flatter slope of the emissivity, $\beta = -2.3$, than the simplest expectation of $\beta = -3$ when a perfectly plain disk is irradiated from a point source with a finite scale height. Another reason for the flat slope is that the index will approach to $\beta = -2$ at outer radii as the scale height of the irradiating source becomes negligible compared with that of the disk.

As mentioned in Section 4.3, the innermost radius obtained from the diskline fit, in units of R_g , are consistent with that independently estimated from the MCD continuum, in units of km, within the uncertainties of the mass function and distance. Comparing our R_{in} value with those obtained in previous observations, we can study how the inner edge of the accretion disk evolves during the low/hard state as a function of luminosity. The 1–100 keV flux during our observations is approximately 14 times brighter than that in the 2008 *Suzaku* observation (Tomsick et al. 2009), which was 2.4×10^{-10} erg $\text{cm}^{-2} \text{sec}^{-1}$. As described in Section 4.3, the R_{in} value ($R_{\text{in}} = 13.3_{-6.0}^{+6.4}$) is at least 5 times smaller within the statistical errors than that obtained in our re-analysis of 2008 data by adopting the common inclination ($i = 50^\circ$) and emissivity index ($\beta = -2.3$). These results indicate that the inner edge moved inward as the luminosity increased from 2008 to 2009.

Table 6 summarizes major previous results on the innermost radius R_{in} of the standard disk of GX 339–4 in different X-ray luminosities and states, all derived from analysis of the iron-K emission line with a relativistic diskline model. We also list other line parameters including the inclination and emissivity index, with which R_{in} could be coupled. The original results obtained by Miller et al.

Table 6. Summary of Previous Results of Iron-K Line Fit Using a Relativistic Disk-line Model.

State	Satellite	$L_{1-100\text{keV}}$ (% L_{Edd})	R_{in} (R_{g})	i (deg)	β	E_{cen} (keV)	Ref.
low/hard	Suzaku+RXTE	0.14	> 65	18 (fixed)	$(-2) - (-3)$	$6.47^{+0.04}_{-0.03}$	[9]
	Suzaku	0.14	190^{+710}_{-90}	50 (fixed)	-2.3 (fixed)	6.4, 7.06 [§] (fixed)	[1]
	Swift+RXTE	0.46	$2.9^{+2.1}_{-0.7}$	20 (fixed)	-3.1 ± 0.4	$6.7^{+0.4}_{-0.3}$	[8]
	Swift+RXTE	1.33	$3.6^{+1.4}_{-1.0}$	20 (fixed)	$-3.2^{+0.6}_{-0.5}$	$6.9^{+0.2}_{-0.5}$	[8]
	Suzaku	2.0	$13.3^{+6.4}_{-6.0}$	46 ± 8	-2.3 ± 0.1	6.4, 7.06 [§] (fixed)	[1]
	XMM-Newton+RXTE	3.25	4.0 ± 0.5	20^{+5}_{-15}	-3.0	6.8 ± 0.1	[5]
	XMM-Newton	3.25	2.8 ± 0.1	$10^{+2}_{-0, \text{pegged}}$	$-3.23^{+0.04}_{-0.05}$	$6.97^{+0.01}_{-0.06}$	[7] [#]
	XMM-Newton	3.25	$6.33^{+1.04}_{-0.08}$	22^{+1}_{-3}	-3.4 ± 2	$7_{-0.02}$	[2] [#]
	XMM-Newton	3.25	24^{+1}_{-4}	60 (fixed)	-3 (fixed)	$6.4^{+0.01}$	[2] [#]
very high	XMM-Newton	12	$2.1^{+0.2}_{-0.1}$	11^{+5}_{-1}	$-5.5^{+0.1}_{-0.5}$	$6.97_{-0.20}$	[4]
	XMM-Newton	12	$1.91^{+0.02}_{-0.01}$	$18.2^{+0.3}_{-0.5}$	$-6.82^{+0.04}_{-0.03}$	$6.97_{-0.01}$	[7] ^{**}
	XMM-Newton+RXTE	12	35^{+25}_{-3}	60 (fixed)			[3] ^{**}
	Suzaku	(28) [*]	~ 1 [†]	18 ± 1	-3.0 ± 0.1		[6]
	Suzaku	(28) [*]	$8.2^{+5.8}_{-3.2}$ [‡]	$33^{+12, \text{pegged}}_{-8, \text{pegged}}$	-3 (fixed)	$6.68^{+0.41}_{-0.47}$	[10] ^{††}

Notes. The errors are 90% confidence level for a single parameter unless otherwise noted.

* 0.5–200 keV Luminosity.

† CDID reflection model convolved with `kerdisk` was used.

‡ 1-sigma confidence limit.

§ Iron $K\beta$ line.

|| Re-analysis of the Tomsick et al. (2009) data.

Re-analysis of the Miller et al. (2006) data.

** Re-analysis of the Miller et al. (2004) data.

†† Re-analysis of the Miller et al. (2008) data.

References. [1] this paper; [2] Done & Diaz Trigo (2010); [3] Kolehmainen et al. (2011); [4] Miller et al. (2004); [5] Miller et al. (2006); [6] Miller et al. (2008); [7] Reis et al. (2008); [8] Tomsick et al. (2008); [9] Tomsick et al. (2009); [10] Yamada et al. (2009)

(2006) in the low/hard state and Miller et al. (2008) in the very high state have been recently re-examined by Done & Diaz Trigo (2010) and Yamada et al. (2009), respectively, and it is pointed out that both data were significantly affected by pile-up. The re-analysis show that the data favor larger values of R_{in} in both cases, although the new constraints become weaker due to poorer photon statistics.

Figure 14 plots R_{in} with its 90% statistical error for a single parameter, as a function of Eddington fraction L_X/L_{Edd} ($D = 8$ kpc and black hole mass of $10M_{\odot}$ are assumed). This figure indicates that the standard accretion disk of GX 339–4 evolves inward as the luminosity increases, with a significant change in the range of $\sim 0.001 < L_X/L_{\text{Edd}} < \sim 0.02$ when the source remains in the low/hard state, as concluded by Tomsick et al. (2009). Our result in the bright low/hard state in 2009 is consistent with that of Done & Diaz Trigo (2010) obtained at a similar luminosity if $R_{\text{in}} \approx 20R_{\text{g}}$. This suggests that at $L_X/L_{\text{Edd}} = 0.02$ the standard disk is likely truncated before reaching to $6R_{\text{g}}$, the ISCO for a non-spinning black hole, although our Suzaku result alone cannot rule out the possibility that the inner edge lies below $6R_{\text{g}}$ at 99% confidence. If GX 339–4 has an extremely-rotating black hole as claimed by Miller et al. (2008), our 2009 result then would be strong evidence that the disk does not extend to the ISCO in the bright low/hard state. Further observations with similar or better energy resolution not limited

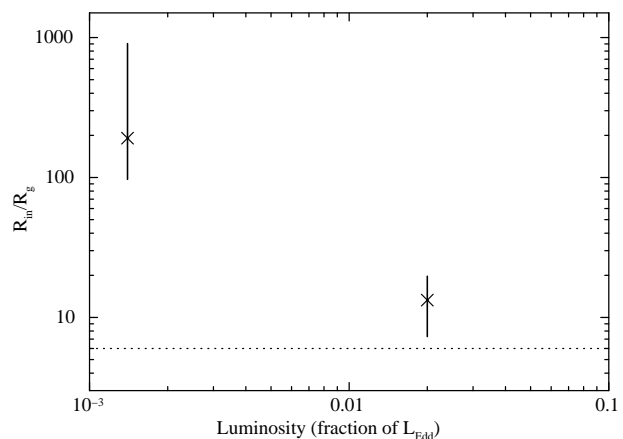


Fig. 14. Estimated innermost radii of the standard disk of GX 339–4 derived from our results from the 2008 (left) and 2009 (right) Suzaku data with an inclination of $i = 50^\circ$ and an emissivity index of $\beta = -2.3$, plotted against fraction of Eddington luminosity (L_X/L_{Edd}).

by the photon statistics and systematic errors caused by pile-up would be necessary to further clarify the right location of the inner edge of the disk in the bright ($\sim 0.01L_{\text{Edd}}$) low/hard state.

6.2. IRSF Results and Jet Energetics

We examine the origin of the multiwavelength SED of GX 339–4 in the low/hard state with different emission components, utilizing our quasi-simultaneous near infrared and X-ray spectra combined with previous data. In the right panel of Figure 13, we plot the estimated contribution of the “intrinsic” MCD component including photons that are Compton-scattered in the corona, through the photon number conservation, assuming that the disk is extending to infinity (for illustrative purpose) with the temperature proportional to $r^{-3/4}$, where r is the radius from the black hole. The results are based on the double CompPS fit, which gives the innermost disk temperature of 0.22 keV. We also plot the upper limit of the contribution from the companion star, assuming a blackbody of 4000 K. Here we refer to the r -band magnitude of > 21.4 by Zdziarski et al. (2004), which is then corrected for extinction corresponding to $A_V = 3.7$. As noticed from the figure, the blackbody component of the multi-color disk and companion star contributes only $\lesssim 0.5\%$ and $\lesssim 1\%$ of the total flux in the near-infrared range, respectively. In the radio band, a slightly inverted power law spectrum is observed with an energy index of $\alpha \approx 0.1$ – 0.2 (Corbel et al. 2000), which is interpreted as an optically thick synchrotron emission from the compact jets, a common feature observed from BHBs in the low/hard state.

Our averaged IRSF spectrum shows a somewhat smaller energy index, $\alpha \approx -0.1$, than the radio spectrum; the corresponding $J - K_s$ color is similar to that of the 1981 observations compiled by Corbel & Fender (2002). As shown by them, this color is consistent with a superposition of two different components with $\alpha = -0.6$ and $\alpha = 2.1$, which can be explained by the optically *thin* synchrotron radiation from the jets and the reprocessed, thermal emission by X-ray irradiation from outer parts of the disk, respectively (see also Markoff et al. 2003; Gandhi et al. 2010). It is thus indicated that the transition point from optically thick to thin regime of the synchrotron emission, defined as ν_t , must appear at frequencies just below or around the near-infrared band, $\sim 10^{14}$ Hz. Note that this conclusion does not match the SSC model discussed by Coriat et al. (2009) for the low/hard state of GX 339–4 where the H band corresponds to an optically *thick* emission in our luminosity range ($L/L_{\text{Edd}} \sim 0.01$ for $M_{\text{BH}} = 10M_{\odot}$ and $D = 8$ kpc). The rapid variability observed in the optical band (e.g., Gandhi et al. 2008) suggests that the power law component of synchrotron radiation extends there, although it is not clear at which frequency the spectrum breaks due to radiative cooling. In our picture, it should be below the X-ray band, since the X-ray flux must be dominated by thermal Comptonization that can well account for the Suzaku spectra.

The observed synchrotron luminosity and the limit for ν_t can be used to constrain the physical parameters of the jet base, from which most of the observed near infrared luminosity is emitted according to the compact jet model (Blandford & Königl 1979). For simplicity, here we consider a single zone model representing this region.

We neglect any effects of relativistic beaming from the bulk motion of the jet, since the Doppler factor is estimated to be $\delta \approx 1.03$ for an inclination of 50° and an assumed intrinsic jet velocity of $0.9c$. Let us assume that the electron number density at the Lorentz factor γ is given as $n(\gamma) = A\gamma^{-p}$ (for $p > 2$) in the range between $\gamma_{\text{min}} < \gamma < \gamma_{\text{max}}$. The synchrotron luminosity density in an optical thin region is expressed as (see e.g., Rybicki & Lightman 1979)

$$\nu L_\nu = \frac{3^{\frac{p+2}{2}}}{2\pi(p+1)} \Gamma\left(\frac{p}{4} - \frac{1}{12}\right) \Gamma\left(\frac{p}{4} + \frac{19}{12}\right) \\ \times V A u_B \sigma_{\text{T}} c \left(\frac{\nu}{\nu_B}\right)^{\frac{3-p}{2}} (\sin\theta)^{\frac{p+1}{2}},$$

where V is the volume ($V = 4\pi R^3/3$ for a sphere with a radius of R), $u_B \equiv B^2/(8\pi)$ is the energy density of the magnetic field, σ_{T} is the cross section of Thomson scattering, $\nu_B \equiv eB/(2\pi mc)$ is the gyro frequency (e and m are the electronic charge and the electron mass, respectively), $\Gamma(y)$ is the gamma function of argument y , and θ is the pitch angle, which is the angle between magnetic field and electron velocity. By assuming equipartition of energy density between the electrons’ kinetic energy and the magnetic field, that is $A = (p-2)u_B/(mc^2)$ with $\gamma_{\text{min}} = 1$, we can estimate the strength of the magnetic field from an observed luminosity for given R and p . Further, using an strict form of the synchrotron absorption coefficient,

$$\alpha_\nu = \frac{(p-2)}{16\pi^2} 3^{\frac{p+3}{2}} \Gamma\left(\frac{3p+2}{12}\right) \Gamma\left(\frac{3p+22}{12}\right) \\ \times u_B^2 \frac{\sigma_{\text{T}}}{m^2 c} \nu_B^{-3} \left(\frac{\nu}{\nu_B}\right)^{-\frac{(p+4)}{2}} (\sin\theta)^{\frac{p+2}{2}},$$

the frequency ν_t below which the synchrotron emission becomes optically thick for a region size of R can be determined from the condition $\alpha_\nu R = 1$. Taking $\nu L_\nu \approx 3 \times 10^{35}$ erg s $^{-1}$ at $\nu = 1.4 \times 10^{14}$ Hz (for $D=8$ kpc), $p = 2.2$ (corresponding to the spectral index $\alpha = (1-p)/2 = -0.6$), and $\nu_t \sim 10^{14}$ Hz, we estimate $B \approx 5 \times 10^4$ G and $R \approx 6 \times 10^8$ cm, which corresponds to $\sim 4 \times 10^2 R_g$. More precisely, dependence of B on R and that of ν_t on B and R are given as

$$B \approx 5 \times 10^4 \left(\frac{\nu L_\nu(K)}{3 \times 10^{35} \text{ erg s}^{-1}}\right)^{\frac{2}{p+5}} \left(\frac{R}{6 \times 10^8 \text{ cm}}\right)^{-\frac{6}{p+5}} \text{ G}$$

and

$$\nu_t \approx 1 \times 10^{14} \left(\frac{B}{5 \times 10^4 \text{ G}}\right)^{\frac{p+6}{p+4}} \left(\frac{R}{6 \times 10^8 \text{ cm}}\right)^{\frac{2}{p+4}} \text{ Hz},$$

respectively, where the terms of the pitch angle are averaged (i.e., integrated over solid angle and normalized by 4π). For this B value, the corresponding energy density of the magnetic field of 8.4×10^7 erg cm $^{-3}$ and the Lorentz factor of electrons emitting the $\nu = 1.4 \times 10^{14}$ Hz photons is $\gamma \approx 40$. Our results hold within a factor of 2 when we assume “particle-dominant” energy balance with $u_e \sim 10u_B$, as observed from jets of blazars (e.g., Inoue & Takahara

1996). The magnetic-field strength in the jet base is consistent with the Giannios (2005) result of $B = 10^5$ G obtained for XTE J1118+480 in the low/hard state from modelling of the multi-wavelengths SED.

Based on these parameters, we roughly evaluate the expected contribution of Compton scattering by the non-thermal electrons, which could produce X-ray and γ -ray photons from seed photons of the synchrotron radiation (synchrotron self Compton; SSC) and external photons (external Compton; EC) from the accretion disk, respectively, for a typical Lorentz factor of $\gamma = 40$. The energy density of synchrotron photons in the near infrared to optical bands is estimated as

$$u_{\text{sync}} \sim L_{\text{sync}} / (4\pi R^2 c) \approx 7 \times 10^6 \text{ erg cm}^{-3},$$

where L_{sync} , which depends on γ_{max} , is assumed to be 10^{36} erg s $^{-1}$. Similarly, that of external photons observed in the X-ray to Gamma-ray bands is

$$u_{\text{Comp}} \sim L_{\text{Comp}} / (4\pi l^2 c) \approx 2 \times 10^6 \text{ erg cm}^{-3},$$

where $L_{\text{Comp}} \sim 2 \times 10^{37}$ erg s $^{-1}$ and the distance from the disk and Comptonized corona to the jet base is assumed to be $l = 5 \times 10^9$ cm that corresponds to the time delay (≈ 150 ms) between the optical and X-ray cross correlation signals (Gandhi et al. 2008).

Thus, the photon energy density of these seed photons is ≈ 10 – 40 times smaller than that of the magnetic field, $u_B = 8.4 \times 10^7$ erg cm $^{-3}$. As noticed from Figure 13, recalling that the ratio of the luminosity between synchrotron and SSC by the same electrons is proportional to u_B/u_{sync} , we estimate that the contribution of Comptonized photons observed in the 1–100 keV X-ray band (SSC) should be approximately 0.4% of the total observed luminosity, which is dominated by thermal Comptonization by the hot corona. This justifies our X-ray spectral model, which ignores any non-thermal emission from the jets. The EC component, however, may contribute to the high energy emission above ~ 1 MeV.

Similarly, we also ignore the jet synchrotron emission as seed photons for thermal Comptonization by the corona in our model, because the emitting regions in the jets are assumed to be distant from the corona and disk. However, we cannot rule out models where the corona and jet base are co-spatial and a Comptonized component of the synchrotron photons significantly contributes to the X-ray emission, as discussed in Markoff et al. (2005). We leave it for future work to apply self-consistent jet and corona models to the simultaneous, multi-wavelengths SED including Suzaku data.

To examine the correlation between the K_s and hard X-ray light curves (Figure 12), we plot the one-day averaged 15–50 keV flux (F_X) versus K_s band flux (F_{K_s}) in Figure 15. The data point taken from the 1981 dataset (Corbel & Fender 2002) is also plotted. By fitting IRSF and Swift points with a power law of $F_{K_s} \propto F_X^\Gamma$, we obtain $\Gamma = 0.45 \pm 0.06$. This value is close to the Coriat et al. (2009) result from GX 339–4 ($0.47 \leq \Gamma \leq 0.49$), which was obtained between the H and 3–9 keV bands. Similar correlation is reported between the radio and X-ray fluxes with a steeper slope of 0.7–0.9 in the low/hard

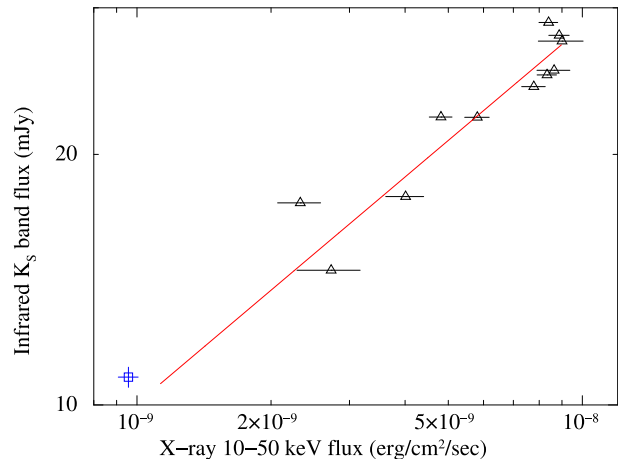


Fig. 15. The relation between the X-ray (15–50 keV) and IR (K_s) fluxes of GX 339–4 with Swift/BAT and IRSF/SIRIUS in 2009 March. The result of the 1997 observation (Corbel & Fender 2002) is also included (blue, open square). Each K_s band flux is calculated by averaging all the magnitudes obtained on the same day. The data points except for the 1997 data are fitted by a power law with $F_{K_s} \propto F_X^\Gamma$. The best-fit result ($\Gamma = 0.45$) is shown as a solid line in this figure.

state (Corbel 2003). These correlations confirm the strong link between the jet formation and accretion flow, as directly indicated by the strong cross correlation between the optical and X-ray bands on much shorter (< 1 sec) time scale for this source.

The slope of the correlation and its dependence on the wavelength and luminosity give us important clues to understand the origin of the SED. As mentioned above, our result is not compatible with models where the near infrared emission is assumed to be an optically thick synchrotron emission. We note that, however, the thermal emission from the irradiated disk must be taken into account as well. Its spectra is represented as a superposition of blackbody radiation that results in a flat SED if the conversion efficiency from the irradiated flux is constant over the whole disk (Frank et al. 2002). The relation between the incident luminosity (L_X) and that of thermal emission from an irradiated outer disk ($L_{\nu, \text{irr}}$) is given by $L_{\nu, \text{irr}} \propto L_X$ at frequencies corresponding to the flat part, and $L_{\nu, \text{RJ}} \propto L_X^{1/4}$ in the Rayleigh-Jeans region (see Coriat et al. 2009). Thus, it is possible that a contribution from the irradiated disk in the Rayleigh-Jeans part could make the observed slope Γ somewhat flatter than those expected from jet models. To prove the origins of the near IR emission, detailed modeling of the complete SED would be necessary, which we leave for our future investigation.

7. Conclusion

We observed GX 339–4 with Suzaku and IRSF in the low/hard state at $\sim 2\%$ of the Eddington luminosity. The conclusions are summarized as follows.

1. The broad-band Suzaku spectra are well represented by a thermal Comptonization by hot ~ 200 keV elec-

trons of seed photons from the optically thick disk, with a small contribution of the direct disk component. The corona has at least two different optical depths, $\tau \approx 0.4$ and 1, indicating inhomogeneous structure.

2. Analysis of the iron-K line with a diskline model yields an innermost radius of $R_{\text{in}} = (13.3^{+6.4}_{-6.0})R_{\text{g}}$ with an estimated inclination of $\approx 50^\circ$.
3. The Suzaku results indicate that the optically thick accretion disk is truncated before the ISCO and its inner regions are almost fully covered by the hot corona. The inferred innermost radii from the continuum fit and the iron-K line profile are consistent each other.
4. The near infrared fluxes are correlated with that of hard X-rays by the relation $F_{\text{Ks}} \propto F_{\text{X}}^{0.45}$, with variable spectral indices from -0.20 to $+0.08$. The spectrum can be explained by a sum of an optically thin synchrotron emission and a thermal emission from the X-ray irradiated outer disk. We estimate the magnetic field and size of the jet base to be 5×10^4 G and 6×10^8 cm, respectively.

This work was partly supported by the Grant-in-Aid for Scientific Research 20540230 (YU), and by the grant-in-aid for the Global COE Program “The Next Generation of Physics, Spun from Universality and Emergence” from the Ministry of Education, Culture, Sports, Science and Technology (MEXT) of Japan. We are grateful to Suzaku operation team for carrying out the ToO observations.

References

- Anders, E., & Grevesse, N. 1989, *Geochim. Cosmochim. Acta*, 53, 197
- Blandford, R. D., & Königl, A. 1979, *ApJ*, 232, 34
- Corbel, S., Fender, R. P., Tzioumis, A. K., Nowak, M., McIntyle, V., Durouchoux, P., & Sood, R. 2000, *A&A*, 359, 251
- Corbel, S., & Fender, R. P. 2002, *ApJ*, 573, L35
- Corbel, S., Nowak, M. A., Fender, R. P., Tzioumis, A. K., & Markoff, S. 2003, *A&A*, 400, 1007
- Coriat, M., Corbel, S., Buxton, M. M., Baily, C. D., Tomsick, J. A., Körding, E., & Kalemci, E. 2009, *MNRAS*, 400, 123
- Cowley, A. P., Schmidtke, P. C., Hutchings, J. B., & Crampton, D. 2002, *AJ*, 123, 1741
- Done, C., Gierliński, M., & Kubota, A. 2007, *A&A Rev.*, 15, 1
- Done, C., & Diaz Trigo, M. 2010, *MNRAS*, 407, 2287
- Esin, A. A., McClintock, J. E., & Narayan, R. 1997, *ApJ*, 489, 865
- Fabian, A. C., Rees, M. J., Stella, L., & White, N. E. 1989, *MNRAS*, 238, 729
- Fender, R., et al. 1999a, *ApJ*, 519, L165
- Fender, R. P., et al. 1999b, *MNRAS*, 304, 865
- Fender, R. P. 2001, *MNRAS*, 322, 31
- Frank, J., King, A., & Raine, D. 2002, *Accretion Power in Astrophysics* 3rd ed., (Cambridge University Press)
- Gallo, E., Corbel, S., Fender, R. P., Maccarone, T. J., & Tzioumis, A. K. 2004, *MNRAS*, 347, L52
- Gandhi, P., et al. 2008, *MNRAS*, 390, L29
- Gandhi, P., et al. 2010, *MNRAS*, 407, 2166
- Giannios, D. 2005, *A&A*, 437, 1007
- Gierliński, M., Zdziarski, A. A., Done, C., Johnson, W. N., Ebisawa, K., Ueda, Y., Haardt, F., & Phillips, B. F. 1997, *MNRAS*, 288, 958
- Hynes, R. I., Steeghs, D., Casares, J., Charles, P. A., & O’Brien, K. 2003, *ApJ*, 583, L95
- Hynes, R. I., Steeghs, D., Casares, J., Charles, P. A., & O’Brien, K. 2004, *ApJ*, 609, 317
- Inoue, S., & Takahara, F. 1996, *ApJ*, 463, 555
- Kaastra, J. S., & Mewe, R. 1993, *A&AS*, 97, 443
- Kolehmainen, M., & Done, C. 2010, *MNRAS*, 406, 2206
- Kolehmainen, M., Done, C., & Diaz Trigo, M. 2011, *MNRAS*, submitted
- Kong, A. K. H., Kuulkers, E., Charles, P. A., & Smale, A. P. 2000, *MNRAS*, 311, 405
- Kubota, A., Tanaka, Y., Makishima, K., Ueda, Y., Dotani, T., Inoue, H., & Yamaoka, K. 1998, *PASJ*, 50, 667
- Kubota, A., & Makishima, K. 2004, *ApJ*, 601, 428
- Lin, D. L., Remillard, R. A., & Homan, J. 2007, *ApJ*, 667, 1073
- Magdziarz, P., & Zdziarski, A. A. 1995, *MNRAS*, 273, 837
- Makishima, K., et al. 2008, *PASJ*, 60, 585
- Markert, T. H., Canizares, C. R., Clark, G. W., Lewin, W. H. G., Schnopper, H. W., & Sprott, G. F. 1973, *ApJ*, 184, L67
- Markoff, S., Nowak, M., Corbel, S., Fender, R., & Falcke, H. 2003, *A&A*, 397, 645
- Markoff, S., Nowak, M. A., & Wilms, J. 2005, *ApJ*, 635, 1203
- Markwardt, C. B., Shaposhnikov, N., Swank, J. H., Altamirano, D., Yamaoka, K., & Ueda, Y. 2009, *ATel*, 1945
- Méndez, M., & van der Klis, M. 1997, *ApJ*, 479, 926
- Miller, J. M., et al. 2004, *ApJ*, 606, L131
- Miller, J. M., Homan, J., Steeghs, D., Rupen, M., Hunstead, R. W., Wijnands, R., Charles, P. A., & Fabian, A. C. 2006, *ApJ*, 653, 525
- Miller, J. M., et al. 2008, *ApJ*, 679, L113
- Mirabel, I. F., & Rodríguez, L. F. 1994, *Nature*, 371, 46
- Mitsuda, K., et al. 1984, *PASJ*, 36, 741
- Mitsuda, K., et al. 2007, *PASJ*, 59, S1
- Muñoz-Darias, T., Casares, J., & Martínez-Pais, I. G. 2008, *MNRAS*, 385, 2205
- Nagayama, T., et al. 2003, *Proc. SPIE*, 4841, 459
- Poutanen, J., & Svensson, R. 1996, *ApJ*, 470, 249
- Reis, R. C., Fabian, A. C., Ross, R. R., Miniutti, G., Miller, J. M., & Reynolds, C. 2008, *MNRAS*, 387, 1489
- Remillard, R. A., & McClintock, J. E. 2006, *ARA&A*, 44, 49
- Rybicki, G. B., & Lightman, A. P. 1979, *Radiative Processes in Astrophysics* (New York: Wiley-Interscience), ch. 6
- Still, M., Brocksopp, C., & Casella, P. 2009, *ATel*, 1954
- Takahashi, H., et al. 2008, *PASJ*, 60, S69
- Tomsick, J. A., et al. 2008, *ApJ*, 680, 593
- Tomsick, J. A., Yamaoka, K., Corbel, S., Kaaret, P., Kalemci, E., & Migliari, S. 2009, *ApJ*, 707, L87
- Ueda, Y., Ebisawa, K., & Done, C. 1994, *PASJ*, 46, 107
- Yamada, S., et al. 2009, *ApJ*, 707, L109
- Zdziarski, A. A., Poutanen, J., Mikołajewska, J., Gierliński, M., Ebisawa, K., & Johnson, W. N. 1998, *MNRAS*, 301, 435
- Zdziarski, A. A., Gierliński, M., Mikołajewska, J., Wardziński, G., Smith, D. M., Harmon, B. A., & Kitamoto, S. 2004, *MNRAS*, 351, 791